# Context-Integrated and Feature-Refined Network for Lightweight Urban Scene Parsing

Bin Jiang<sup>1</sup>, Wenxuan Tu<sup>1</sup>, Chao Yang<sup>1</sup>, and Junsong Yuan<sup>2</sup>

Hunan University, Changsha, China

State University of New York at Buffalo, NY, USA

Abstract—Semantic segmentation for lightweight urban scene parsing is a very challenging task, because both accuracy and efficiency (e.g., execution speed, memory footprint, and computation complexity) should all be taken into account. However, most previous works pay too much attention to one-sided perspective, either accuracy or speed, and ignore others, which poses a great limitation to actual demands of intelligent devices. To tackle this dilemma, we propose a new lightweight architecture named Context-Integrated and Feature-Refined Network (CIFReNet). The core components of our architecture are the Long-skip Refinement Module (LRM) and the Multi-scale Contexts Integration Module (MCIM). With low additional computation cost, LRM is designed to ease the propagation of spatial information and boost the quality of feature refinement. Meanwhile, MCIM consists of three cascaded Dense Semantic Pyramid (DSP) blocks with a global constraint. It makes full use of sub-regions close to the target and enlarges the field of view in an economical yet powerful way. Comprehensive experiments have demonstrated that our proposed method reaches a reasonable trade-off among overall properties on Cityscapes and Camvid dataset. Specifically, with only 7.1 GFLOPs, CIFReNet that contains less than 1.9 M parameters obtains a competitive result of 70.9% MIoU on Cityscapes test set and 64.5% on Camvid test set at a real-time speed of 32.3 FPS, which is more cost-efficient than other stateof-the-art methods.

Index Terms—Semantic Segmentation, Urban Scene Parsing, Model Efficiency, Multi-scale Contexts.

#### I. INTRODUCTION

Semantic segmentation aims at labeling pixel-level signals associated with object category, location, and shape for a specific scenario, which can be utilized in many applications such as robotic system, driving perception, and medical imaging [1]-[3]. Specially, urban scene parsing of driving perception is supposed to segment the whole image into different semantic parts such as a building, a car, and a person, as shown in Fig. 1. The core challenge of this task is how to keep a high accuracy and decent execution speed under resource constraints. Hence for algorithms to be practically applicable, it is necessary that they have to be resource-saving, fast, as well as obtain a promising accuracy.

Early Convolutional Neural Networks (CNNs) based works [4]-[10] manage to handle this task by U-shape or Multi-scale design, which can make full use of spatial information or contexts for achieving high accuracy, as shown in Fig. 2(a) and Fig. 2(b). However, these algorithms rely on more convolutions and sophisticated operations, which are time-consuming and require enormous computation resources. For example, even though the skip learning strategy in U-shape architecture

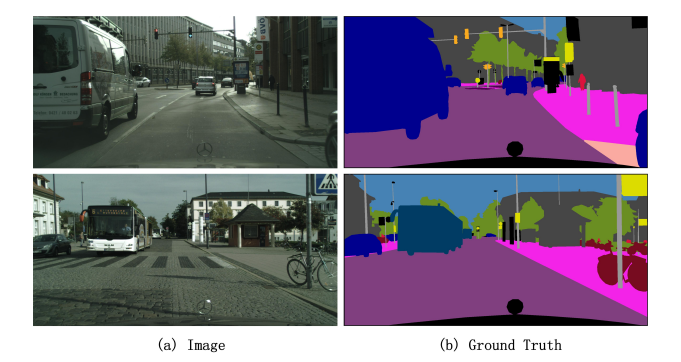


Fig. 1. Illustration of some representative urban scenes in Cityscapes dataset. An autonomous vehicle must comprehensively implement driving scene interactivity with the complex traffic environment, then make the driving decision timely.

benefits details recovery, each layer in encoder transfers an equivalent number of feature maps to corresponding layer in decoder, which demands large amounts of extra computations [3]-[6]. Moreover, obtaining multi-scale contexts on the tail of the Res101-based network would help solve challenging scene variations and boost performance eventually, but at the expense of 2,048 feature maps computed by  $3 \times 3$  regular convolution before feature integration [8]-[10]. To overcome these shortcomings, a series of works have sparked a trend toward designing model in real-time and lightweight needs [11]-[13]. As illustrated in Fig. 2(c), a typical architecture of asymmetric encoder-decoder focus on reducing the number of parameters for acceleration. Nevertheless, most of them heavily compromise accuracy to speed by compressing feature channels, resulting in the final MIoU (Mean Intersection over Union) score notably drops to 60% and even lower [12], [13].

Recently, there has been increasing interest in jointly considering a good trade-off between accuracy and speed [14]-[18]. Though state-of-the-art methods can meet the real world requirements that the intelligent devices should make fast and accurate decision in response to the specific scene, we argue that most of them take less consideration on other importance factors (e.g., space constraints or computation requirements). For instance, ERFNet [16] employs factorized convolutions with different dilation rates in encoder to maintain the accuracy-speed balance. Unfortunately, multiple regular transposed convolution layers in decoder may suffer from amounts of invalid floating point operations. Also, it can only handle single scale cases due to fixed-size field of view

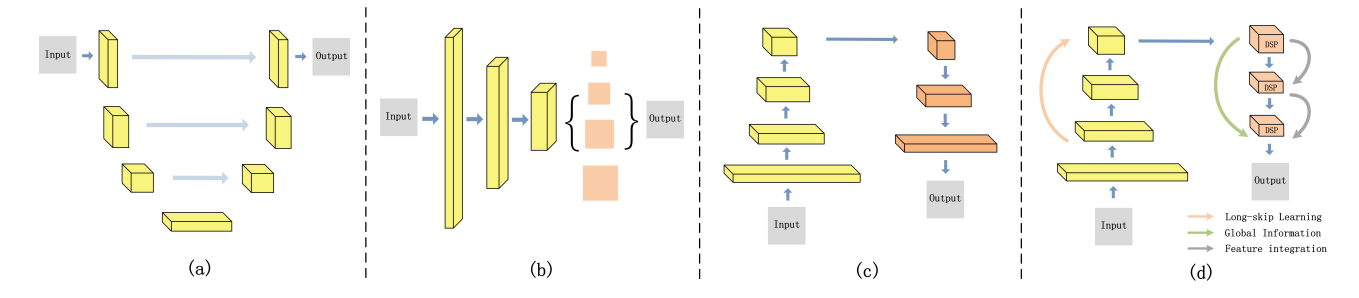


Fig. 2. Architecture comparison. From left to right: (a) U-shape. (b) Multi-scale contexts. (c) Asymmetric encoder-decoder. (d) Our proposed CIFReNet.

in each layer, let alone spatial details. In order to address these drawbacks, another strategy [17] follows the principle of multi-branch framework to process multi-resolution inputs, then gathers them by a feature integration module. Although it seems cost-effective, the additional branches based on regular CNNs bring large amounts of redundant parameters.

According to aforementioned analysis in the field of urban scene parsing, there has been far less attention to take an overall performance into consideration. To address these issues, a highly challenging demand has been raised for algorithms that are not only required to perform high accuracy and fast speed, but also they are required to process signals on low-power intelligent devices. This motivates a question: how to take the advantages of quality-finer and speed-faster algorithms for our model design in an economic yet effective way?

In this paper, we establish a lightweight architecture called Context-Integrated and Feature-Refined Network (CIFReNet), which is specifically tailored for resource constrained environments, as can be seen in Fig. 2(d). Our CIFReNet mainly involves two components: Long-skip Refinement Module (LRM) and Multi-scale Contexts Integration Module (MCIM). In pursuit of a better accuracy, we firstly adopt a single longskip connection between shallow layer and deep layer as a highway, in order to ease the propagation of low-frequency information and narrow the gap between multi-level features. Then we apply channel attention mechanism, which adaptively revises some crucial details to further refine segmentation results. After that, Dense Semantic Pyramid (DSP) blocks, as the basic units of MCIM, are elaborately designed to aggregate multi-perspective clues together at different dilation rates. Meanwhile, global prior knowledge is added into MCIM, so as to enlarge the field of view. Thus, MCIM learns the joint information of both local and global contexts, which guides the learning process more precisely. From the perspective of model efficiency, our CIRFNet only contains 22 depth-wise separate convolution layers [19], and the maximum number of each block is no more than 320, which maintains the model execution speed and guarantees the adequate information during propagation simultaneously. To further reduce redundant parameters and invalid floating point operations, depth-wise separable convolution [20] and group convolution [21] are used to optimize our LRM and MCIM. Note that DSP blocks are stacked in cascade rather than in parallel, refraining from large number of channels after feature integration. Finally, the prediction maps are bilinearly upsampled directly without any additional branch or transposed convolution layer, thus greatly improving the resource utilization ratio. We rigorously demonstrate that our CIFReNet obtains 70.9% MIoU on Cityscapes *test* set and 64.5% on Camvid *test* set with less than 1.9 M parameters and only 7.1 GFLOPs. Meanwhile, it processes an image of 1,024 × 512 resolution at a speed of 32.3 FPS on a single NVIDIA GTX 1080Ti card. Compared with other state-of-the-art competitors, our method could reach a reasonable trade-off among overall properties.

The key contributions of this paper are three-fold:

- A cost-efficient prototype named CIFReNet is proposed for urban scene parsing. Compared with current stateof-the-art approaches, our method obtains a more comprehensive trade-off among accuracy, execution speed, memory footprint, and computation complexity. As a side contribution, we will release our source codes.
- A slight yet effective LRM is designed, which adopts a long-skip connection with channel attention mechanism to provide a highway and a proper guidance for spatial information learning. Therefore, it can adaptively refine segmentation results in a coarse level for better accuracy.
- An efficient and powerful MCIM with cascaded DSP blocks is presented, so as to generalize the use of multiperspective contexts and expand the field of view. In particular, the DSP block can encode much denser semantic information with an acceptable cost.

The remainder of this paper is organized as follows. Section II reviews related works on semantic segmentation in terms of lightweight-oriented and accuracy-oriented approaches. Section III presents the model design and each component of our model. Section IV conducts experiments and discusses the results. Finally, section V draws a conclusion.

## II. RELATED WORK

Some recent works based on Fully Convolution Networks (FCNs) [22] have achieved promising results on public benchmarks [23], [24]. We then review the latest deep-learning-based methods from lightweight-oriented and accuracy-oriented aspects for scene parsing tasks.

# A. Lightweight-oriented Approaches

Lightweight semantic segmentation algorithms [11]-[18] aim at solving the problem of slow speed and resource constraints on intelligent devices. These works can be roughly

divided into two types: speed-fast structure and accuracyspeed trade-off structure. As for the former, examples include ENet [12], which employs the combination of an initial block and a group of factorizing filters for acceleration. Based on this, ESPNet [13] assembles Efficient Spatial Pyramid (ESP) modules into an encoder-decoder structure, outperforming ENet in terms of accuracy and speed. Although efforts have been made on designing an extremely speed-fast and resourcesaving model, most of these algorithms sacrifice too much accuracy, so they can not provide sufficient precise information to guarantee safe autonomous driving. The latter type tries to balance the accuracy and speed, it has become an active research area in the last few years. Specifically, ERFNet [16] substantially applies a convolutional factorization technique to make parameters less redundant, and obtains acceptable accuracy. Besides, ICNet [17] designs multi-branch cascaded networks for a fast execution speed, and then applies multiscale resolution for coarse-to-fine inference. Despite their success, so far most of them have taken less consideration on either space constraints or computation requirements, which are unfeasible for intelligent devices requiring low memory footprint and computation complexity. Different from the aforementioned works, our lightweight CIFReNet performs a promising accuracy by LRM and MCIM, and makes efforts to take account of overall efficiency.

# B. Accuracy-oriented Approaches

Towards a high-quality result, most accuracy-oriented approaches are designed to encode more spatial information and contexts.

1) Feature Refinement: Refining spatial information is a common challenge in semantic segmentation algorithms [3]-[6], [25], [26], which plays an important role in predicting the pixel-level localization. A direct solution as employed in U-Net [3], is to design a symmetrical encoder-decoder model, which adopts long-skip connections to refine details by fusing the hierarchical features of backbone. Similarly, SegNet [4] introduces a typical U-Shape structure and utilizes the saved pooling indices to compensate the spatial information for highlevel features gradually. This idea has been also presented in [5] and [6], the authors create an up-sampling stage corresponding to each down-sampling one, and fuse them in the decoder layer by layer. However, most of them straightly adopt element-wise addition or channel concatenation to bridge the gap among multi-level features step by step, resulting in both high computation burden and less efficiency of feature representations. In contrast, we adopt a simple long-skip residual learning module to keep low-frequency information easier bypassed from bottom to top. Meanwhile, we introduce more semantic information to guide the low-frequency features learning, which refines the final segmentation effectively with only a slight computation increase.

2) Multi-scale Contexts Integration: Multiple contexts are generally seen as a key factor in current researches [7]-[10], [27]-[31], which help to provide a good descriptor for overall scene interpretation. Among them, PSPNet has exhibited an impressive performance by adopting Spatial Pyramid

#### TABLE I

NETWORK ARCHITECTURE. LRM: LONG-SKIP REFINEMENT MODULE. GAP: Global Average Pooling.  $\mathrm{DSP}_k$ : Dense Semantic Pyramid,  $D_k$ : Dilaion rates,  $k \in (s, m, l)$ .  $C_o$ : Output channels. C: The number of categories. ULL: Upsampling Logits Layer.

Model	Dilation	$C_{o}$	Outsi	ze	Repeat
Model	Dilation	0	Cityscapes	Camvid	Керсаі
Stage0	1	32	1,024 × 512	240 × 180	1
Stage1	1	16	$1,024 \times 512$	$240 \times 180$	1
Stage2	1	24	$512 \times 256$	$120 \times 90$	2
Stage3	1	32	$256 \times 128$	$120 \times 90$	3
LRM	-	160	$256 \times 128$	$120 \times 90$	1
Stage4	2	64	$256 \times 128$	$120 \times 90$	4
Stage5	3	96	$256 \times 128$	$120 \times 90$	3
Stage6	5	160	$256 \times 128$	$120 \times 90$	3
Stage7	7	320	$256 \times 128$	$120 \times 90$	1
GAP	-	200	-	-	-
$DSP_s$	$D_s$	200	$256 \times 128$	$120 \times 90$	1
$\mathrm{DSP}_m$	$D_m$	200	$256 \times 128$	$120 \times 90$	1
$DSP_l$	$D_l$	200	$256 \times 128$	$120 \times 90$	1
ULL	-	C	$2,048 \times 1,024$	$480 \times 360$	1

Pooling (SPP) module for capturing abundant contexts [7], while DeepLab V2 integrates multi-scale contexts via utilizing Atrous Spatial Pyramid Pooling (ASPP) module at diverse dilation rates [8]. Following the same spirit, [9] embeds global features into local contexts for the purpose of a larger field of view. Further, Ding et al. [27] try to selectively integrate multiscale features for each spatial position by a scheme of gated sum. Subsequently, Zhang et al. [28] design a scale-adaptive convolution to exploit long-range contexts, acquiring a flexible size of receptive field. Although these algorithms perform well in solving the challenge of scene variations, most of them prefer heavy backbones and complicated modules to pursue a high accuracy. During scene parsing, these defects cause the time-consuming inference and much heavy overheads. In order to alleviate this problem, we propose the MCIM, which adequately utilizes local and global contexts for better scene parsing with negligible impact on computation cost.

#### III. METHOD

# A. Overview

In this section, we present a single-shot architecture called CIFReNet for lightweight urban scene parsing, which mainly consists of a Long-skip Refinement Module and a Multi-scale Contexts Integration Module. It aims to achieve an overall trade-off in terms of accuracy, execution speed, memory footprint, and computation complexity by efficiently learning spatial and contextual information.

As depicted in Fig. 3, given an image of urban scene, we firstly feed it into our backbone network, namely modified MobileNet V2 to obtain semantic features. The Output Stride (OS) of our backbone is reasonably set to 8 and 4 for Cityscapes [23] and Camvid [32] datasets respectively, so as to preserve more details and keep the memory usage in check. Furthermore, we replace the last four sub-sampling operations with dilation convolutions, and apply a group of dilation rates {2, 3, 5, 7} alternately to maintain the field of view, as illustrated in Table I. Note that all initial settings mentioned above are verified according to ablation experiments.

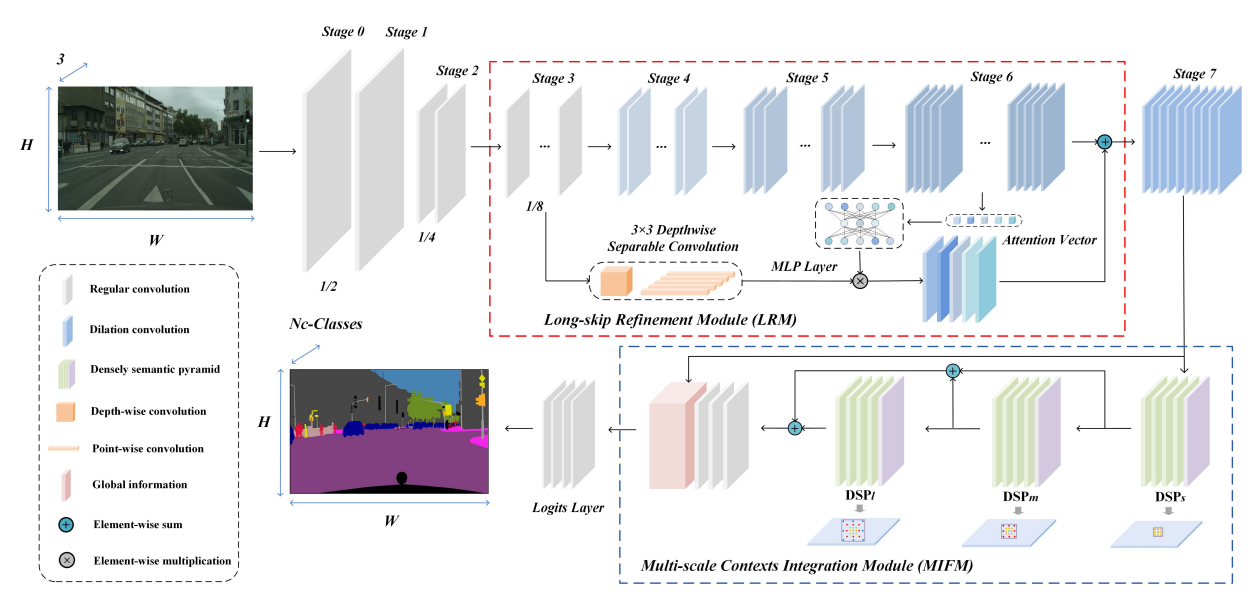


Fig. 3. An overview of Context-Integrated and Feature-Refined Network (CIFReNet). The dotted red box and blue box represent the Long-skip Refinement Module (LRM) and the Multi-scale Contexts Integration Module (MCIM), respectively.

Next, we perform a Long-skip Refinement Module, as shown in the red box of Fig. 3. For the first step, we apply a simple long-skip connection between spatial layer and semantic layer. The high-dimensional spatial features are generated by a simple  $3\times 3$  depth-wise separate convolution. For the second step, the high-level features are transformed into a group of weight vectors and used to refine the high-dimensional spatial features. Through the above process, we perform an element-wise addition operation on the above refined features and high-level features. Such a design eases the propagation of low-frequency information and boosts the quality of feature refinement, which facilitates a better segmentation result with richer details. Meanwhile, it only contains a slight long-skip connection. Thus, it brings negligible overheads.

Thereafter, to gather both local and global contexts, we feed semantic features outputted from the tail of the backbone into Multi-scale Contexts Integration Module. As shown in the blue box of Fig. 3, three lightweight DSP blocks with a global constraint are piled up in the network. Such a cascaded design has two advantages. On the one hand, it facilitates enlarging the field of view by increasing the depth of network. On the other hand, it follows the principle of "deep and thin" [33], which considerably boosts the model efficiency. Additionally, the output semantic features from each DSP block are integrated together, which allows the network to jointly learn contexts at multi-level scales for a better recognition capacity.

Finally, we directly up-sample the output back to full resolution after Logits Layer (LL). In the following sections, we will elaborate how LRM and MCIM facilitate obtaining a better result in an economic yet effective way. Besides, we summarize all notations in Table II.

TABLE II
BASIC NOTATIONS FOR THE PROPOSED METHOD.

Notations	Meaning			
$H \times W$	The size of feature maps			
$C_i$	The number of input channels			
$C_o$	The number of output channels			
$F_s$	The low-dimensional shallow feature maps			
$f_{sc}^{H  imes W}$	The $c$ -th feature map of $F_s$			
$F_s'$ $f'H \times W$	The high-dimensional shallow feature maps			
$f'_{sc'}^{H\times W}$	The $c'$ -th feature map of $F'_s$			
$F_a$	The high-dimensional abstract feature maps			
$f_{ac'}^{H \times W}$	The $c'$ -th feature map of $F_a$			
V	The set of attention vectors for $F_s'$			
$v_{c'}^{1\times 1}$	The $c'$ -th attention vector of $V$			
$I_n^{H \times W \times C_i}$	The input of <i>n</i> -th DSP			
$I_{n}^{'H\times W\times (C_{o}\times r)}$	The channel-reduced feature maps of <i>n</i> -th DSP			
$L_n$	The set of k-groups features in n-th DSP			
$l_{nk}^{H \times W \times (C_o \times r), d_{nk}}$	The $k$ -th group features of $L_n$			
$D_n$	The set of dilation rates in <i>n</i> -th DSP			
$d_{nk}$	The dilation rate of $k$ -th group in $n$ -th DSP			
$g' \stackrel{H \times W \times (C_o \times r)}{n}$	The global feature maps in <i>n</i> -th DSP			
$O_n^{H \times W \times C_o}$	The output of <i>n</i> -th DSP			
$O'_{n}^{H \times W \times C_{o}}$	The residual output of <i>n</i> -th DSP			
$\frac{F_{stage7}^{H \times W \times C_i}}{g_{"n}^{H \times W \times C_o}}$	The semantic feature maps of stage 7			
$g_{"n} \overset{H \times W \times C_o}{\underset{n}{\bigvee}}$	The global contexts from $F_{stage7}^{H \times W \times C_i}$			
$O^{''H\times W\times 2\times C_o}$	The output of MICM			

#### B. Long-Skip Refinement Module (LRM)

As discussed in Section I, the U-shape architecture indicates that skip learning is beneficial to model performance improvement, but suffers from low speed and double resource utilization. Therefore, inspired by the success of long-skip learning [34] and channel attention mechanism [35], we introduce Long-Skip Refinement Module to enhance the network learning capacity with marginal extra computation cost.

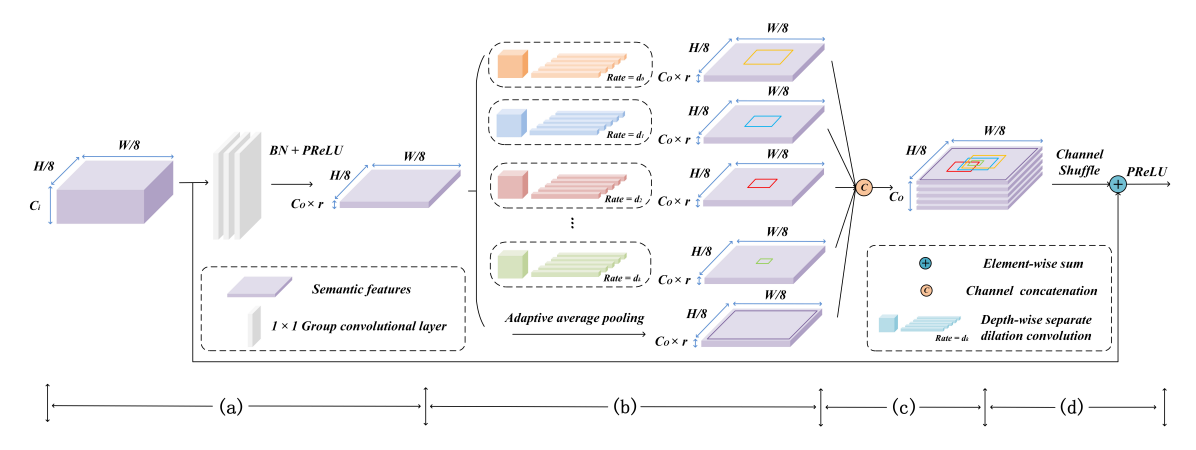


Fig. 4. Overview of the Dense Semantic Pyramid (DSP) block. (a) Channel reduction. (b) Dense dilation sampling. (c) Semantic features integration. (d) Channel shuffle operation.

1) Basic long-skip learning: According to our observations, different layers of neural networks exhibit different feature expression capabilities. On the one hand, in the shallower stages, the network could encode finer spatial information but contain much noise. On the other hand, although the deeper stages could provide more semantic information, it loses too many visual details. In our ablation experiments, we find that performing LRM between stage 2 and stage 7 delivers a better trade-off compared with other options, which contains ten inverted residuals (as illustrated in Table I) in total.

As depicted in the red box of Fig. 3, given shallow feature maps (outputted from stage 3) as an input  $F_s = \{f_{s0}^{H \times W}, f_{s1}^{H \times W}, \cdots, f_{sc}^{H \times W}\}$ , where  $c \in \{0, 1, \cdots, C_{i}\text{-}1\}, F_s \in \mathbb{R}^{H \times W \times C}$ , we firstly apply a simple depth-wise separable convolution layer to transform low-dimensional  $F_s$  into high-dimensional  $F_s' = \{f_{s0}^{H \times W}, f_{s1}^{H \times W}, \cdots, f_{sc'}^{H \times W}\}$ , where  $c' \in \{0, 1, \cdots, C_o\text{-}1\}, F_s' \in \mathbb{R}^{H \times W \times C}$ , which is beneficial to feature representations but not computation expensive, as described in Eq. (1). Then we fuse  $F_s'$  and abstract features (outputted from stage 6)  $F_a = \{f_{a0}^{H \times W}, f_{a1}^{H \times W}, \cdots, f_{ac'}^{H \times W}\}$ , where  $c' \in \{0, 1, \cdots, C_o\text{-}1\}, F_a \in \mathbb{R}^{H \times W \times C}$  by elementwise addition, which serves as our basic long-skip structure for residual learning. By this way, more abundant low-frequency information can be bypassed conveniently in the network.

$$f^{'H\times W}_{sc^{'}}=\delta(pw^{1\times 1}\times\delta(dw^{3\times 3}\times f^{H\times W}_{sc}+b)+b), \quad \ (1)$$

where  $dw^{3\times3}$  and  $pw^{1\times1}$  are defined as a 3 × 3 depth-wise convolution and a 1 × 1 pointwise convolution, respectively. b represents bias vector.  $\delta(\cdot)$  indicates the operations of both Batch Normalization (BN) [36] and Parametric Rectified Linear Unit (PReLU) [37] function.

2) Spatial feature refinement: Though Zhang et al. [34] have proven that long-skip connection not only eases the optimization process but also promotes network learning in a coarse level, we argue that straightly embedding shallow features along with much noise into valuable semantic features is meaningless. To regularize the otherness, our idea is involving high-level features to provide a helpful constraint for low-level features rather than simply performing element-wise addition or concatenation. Based on this intuition, we then

reshape high-level feature maps  $F_a$  into an attention vector  $V = \{v_0^{1\times 1}, v_1^{1\times 1}, \cdots, v_{c'}^{1\times 1}\}$ , where  $c' \in \{0, 1, \cdots, C_o\text{-}1\}$ , via a global average pooling layer and simple linear layers, similar to SENet [35]. Finally, a softmax layer is applied to calculate the response value which allows  $F_s'$  to adaptively adjust its selection. We present this process as follows:

$$v_{c'}^{1\times 1} = \frac{1}{H \times W} \sum_{i=1}^{H} \sum_{j=1}^{W} f_{ac'}(i,j),$$
 (2)

$$O_{c'}^{H \times W} = \frac{exp(MLP(v_{c'}^{1 \times 1}))}{\sum_{i=0}^{C_o-1} exp(MLP(v_i^{1 \times 1}))} \otimes f_{sc'}^{'H \times W} \oplus f_{ac'}^{H \times W}, \tag{3}$$

where  $MLP(\cdot)$  denotes Multi-Layer Perception.  $\otimes$  and  $\oplus$  refers to element-wise multiplication and addition, respectively.

# C. Multi-scale Contexts Integration Module (MCIM)

In the task of scene parsing, most current algorithms apply multi-scale modules such as PPM [7] and ASPP [8] to effectively deal with scene variations, but decrease the model execution efficiency. To overcome this limitation, our Multi-scale Contexts Integration Module which consists of three DSP blocks and global information, is designed within a "deep and thin" scheme to achieve better efficiency, as shown in blue box of Fig. 3. Our MCIM has only **0.13 M** parameters and requires fewer resource utilization (**0.53 MB** and **1.80 GFLOPs**). Next, we conduct further analysis about both efficiency and effectiveness of it.

1) Dense Semantic Pyramid (DSP): The Dense Semantic Pyramid block, with less than **0.024 M** parameters, is specifically designed for context extraction as the core component of MCIM. We then will reveal the design of DSP block in detail as the following four steps.

Lightweight convolutional techniques. As we know, depth-wise separable convolution [20] and group convolution [21] have been proven more efficient (in terms of memory needed and computation complexity) while keeping an accuracy equivalence compared to the regular convolution. To make our DSP block more computationally efficient, we take advantages of them for a flexible usage. As

#### TABLE III

Type	#Par(M)
RC	$C_i \times C_o \times m^2 = 0.576$
GC	$(C_i \times C_o \times m^2)/g = 0.144$
DSC	$1 \times C_i \times m^2 + C_i \times C_o \times 1 \times 1 = 0.067$
RC-DSP	$(C_i \times (C_o \times r)) + m^2 \times (C_o \times r)^2 \times K = 0.106$
DSP	$(C_i \times (C_o \times r))/g + ((C_o \times r) \times m^2 + (C_o \times r)^2) \times K = 0.016$

displayed in Fig. 4, given feature maps  $I_n^{H \times W \times C_i}$  as the input of the *n*-th DSP block, where  $I_n^{H \times W \times C_i} \in \mathbb{R}^{H \times W \times C}$ , we firstly feed it into a single  $1 \times 1$  group point-wise convolution followed by BN and PReLU activation, to obtain channel-reduced feature maps  $I_n^{H \times W \times (C_o \times r)}$ , where  $I_n^{H \times W \times (C_o \times r)} \in \mathbb{R}^{H \times W \times C}$ , and r refers to channel reduction ratio. Then they are successively sent to K parallel depth-wise separable convolutions followed by BN and PReLU as well, to generate K groups feature maps  $L_n = \{l_{n0}^{H \times W \times (C_o \times r), d_n}, \ l_{n1}^{H \times W \times (C_o \times r), d_n}, \ \dots, \ l_{nk}^{H \times W \times (C_o \times r), d_n}\}$ in the *n*-th DSP block, where d denotes dilation rate,  $k \in \{0,$ 1,  $\cdots$ , K-1. As following these lightweight convolutional techniques [20], [21], the dense convolution between all channels is uniformly changed to be sparse, so that calculating low-dimensional feature maps is affordable under a given resource budget. As listed in Table III, top three rows of the table compares the regular convolution against lightweight convolutions, while bottom two rows of the table clearly shows that the design of DSP block is more beneficial, by receiving a 6.7 times reduction in parameters compared with the regular one.

Denser dilation sampling. After that, all neurons in each branch share the same field of view at a single scale. However, we are supposed to give different perspectives to them, because pixels near the target usually contain more related semantic information, which helps us to get enough local contexts for better accuracy. To gather the local neighboring information as many descriptors as possible, we successively replace original dilation rates in  $3 \times 3$  depthwise convolutions with a group of coprime dilation rates (inspired by the prior work [38])  $D_n = \{d_{n0}, d_{n1}, \dots, d_{nk}\},\$ where  $k \in \{0, 1, \dots, K-1\}$ , and n is the n-th DSP block. Compared with the case in Fig. 5(a), a much denser measure is provided for incorporating more relevant sub-regions  $L_n = \{l_{n0}^{H\times W\times (C_o\times r),d_{n0}},\ l_{n1}^{H\times W\times (C_o\times r),d_{n1}},\cdots,l_{nk}^{H\times W\times (C_o\times r),d_{nk}}\}$ in the *n*-th DSP block, where  $k \in \{0, 1, \dots, K-1\}$ . In this way, it can enrich the feature representations without any extra parameters, as depicted in Fig. 5(b). Here we emphasize, although the operation of channel reduction dramatically decreases the computation cost and K provides multiple options to obtain more confident results, we reasonably set r to 0.2 and K to 4 by performing ablation studies, which avoids performance degradation due to much information loss. The above process can be formulated as:

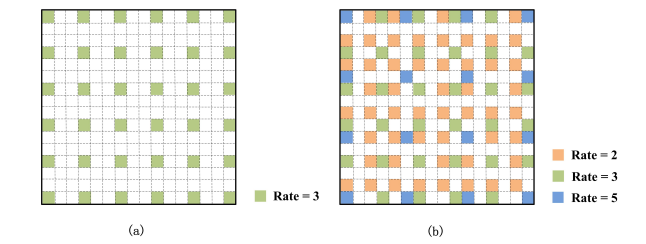


Fig. 5. Dilation sampling comparison. (a) Sparse Feature Sampling. (b) Denser Feature Sampling.

$$I_{n}^{'H\times W\times (C_{o}\times r)} = \delta(w_{n}^{1\times 1} \times I_{n}^{H\times W\times C_{i}} + b_{n}), \quad (4)$$

$$l_{nk}^{H\times W\times (C_o\times r),d_{nk}} = \delta(pw_{nk}^{1\times 1} \times \delta(dw_{nk}^{3\times 3,d_{nk}} \times I_n'^{H\times W\times (C_o\times r)} + b_{nk}) + b_{nk}).$$
 (5)

**Local and global contexts extraction.** Our DSP block with different dilation rates performs to perceive patches or pixels locally, but falls short of a global view, especially for parts of large regions and confusion categories. To remedy this defect, we directly obtain global contexts  $g_n^{H\times W\times (C_o\times r)}$  from feature maps  $I_n^{H\times W\times (C_o\times r)}$  by adopting a global average pooling (GAP) layer with small computation overheads, similar to [9]. Thereafter, the features are integrated from all parallel paths. Please note that directly integrating them stemmed from a group convolution layer may weaken feature representations [21]. Consequently, a channel shuffling operation is applied to ease cross-group information  $O_n^{H\times W\times C_o}$ , where  $O_n^{H\times W\times C_o}\in\mathbb{R}^{H\times W\times C}$ , as formulated below:

$$g_{\prime n}^{H \times W \times (C_o \times r)} = U(G(I_n^{\prime H \times W \times C_o \times r)})), \qquad (6)$$

$$O_n^{H \times W \times C_o} = S(C[l_{n0}^{H \times W \times (C_o \times r), d_{n0}}, l_{n1}^{H \times W \times (C_o \times r), d_{n1}}, \dots, l_{nk}^{H \times W \times (C_o \times r), d_{nk}}], g_{\prime n}^{H \times W \times (C_o \times r)}), \qquad (7)$$

where  $G(\cdot)$  denotes a global average pooling layer,  $U(\cdot)$  represents upsampling transformation by bilinear interpolation.  $C[\cdot \cdot \cdot]$  means the feature concatenation, and  $S(\cdot)$  corresponds to a channel shuffling operation.

**Short-skip residual learning.** To further speed up the convergence of deep neural networks, we adopt a shortcut connection that strengthens gradient back-propagation in our DSP block, inspired from the principle of ResNet [39]. Formally, the combination of input  $I_n^{H\times W\times C_i}$  and non-linear transformation output  $O_n^{H\times W\times C_o}$  is described as:

$$O_n^{'H\times W\times C_o} = I_n^{H\times W\times C_i} \oplus O_n^{H\times W\times C_o} \text{ s.t. } C_i \equiv C_o.$$
 (8)

2) Going Deeper with a Global View: Towards the purpose that both model efficiency and the field of view are important, we cascade three DSP blocks and add a global view at the end of the last DSP block in MCIM, as illustrated in Fig. 3.

**Deep and thin schema.** In contrast to previous multi-scale networks [7]-[10] which calculate large number of feature maps in a parallel-branch module, we stack three DSP blocks in cascade to save the computation cost as much as possible. Moreover, we follow the strategy of pixel sampling rates in ASPP but keep them more denser in our DSP blocks. As Fig. 3 shows, each DSP block has its own function individually.

Specifically, the first one with a group of dilation rates  $D_s = \{1, 2, 3, 5\}$  mainly pays more attention to small size objects (e.g., traffic sign). On the basis of the former, we employ the second DSP block with a group of dilation rates  $D_m = \{7, 9, 11, 13\}$  to focus on medium size objects (e.g., car). Furthermore, the last DSP block with a group of dilation rates  $D_l = \{17, 19, 21, 23\}$  takes large size objects (e.g., train or truck) into account. It is worth mentioning that since high-level feature maps contain a limited number of channels and the resolution of them is small, using large dilation rate does not bring too much resource utilization. Finally, we combine the prediction of each DSP block to jointly encode multi-level semantics for better accuracy, in a similar spirit as in FCN [22].

**Enlarging the field of view.** As formulated in Eq. (11) and Eq. (12), each descriptor with dilation rate D and kernel size K in DSP blocks preserves a field of view R. Therefore, stacking all DSP blocks together can theoretically obtain the largest receptive field  $R_{max}$ :

$$R = (D-1) \times (K-1) + 1, \tag{9}$$

$$R_{max} = R_{max}^s + R_{max}^m + R_{max}^l - 2, (10)$$

for instance, our multi-scale module will result in a receptive field of maximum size 77 for local contexts.

However, we argue that in practice, the size of an effective field of view is smaller, resulting from amounts of abandoned information (e.g., marginal areas of feature maps) as the network goes deeper. To handle this problem, we add a slight GAP layer on the tail of the backbone. Then the global information is directly combined with integrated semantics. Therefore, our MCIM can allow our model to extract global responses  $g_{\prime\prime}{}_{n}^{H\times W\times C_{o}}$  from  $F_{stage7}^{H\times W\times C_{i}}$ , which keeps the valid field of view large enough from a more macroscopic aspect. This process can be expressed as:

$$g_{"n}^{H \times W \times C_o} = U(G(\delta(w^{1 \times 1} \times F_{stage7}^{H \times W \times C_i} + b_n))),$$
 (11)

$$O^{"H \times W \times 2 \times C_o} = C[O_s^{H \times W \times C_o} \oplus O_m^{'H \times W \times C_o}]$$

$$\oplus O_l^{'H \times W \times C_o}, g_{"n}^{H \times W \times C_o}]. \tag{12}$$

# IV. EXPERIMENTAL EVALUATION

To validate the performance of our network, we detailedly present an experimental procedure as below.

# A. Training Protocol

1) Dataset: Cityscapes Dataset. The Cityscapes is a popular dataset for urban scene parsing [23]. It consists of 25,000 annotated  $2,048 \times 1,024$  resolution images. The dense annotation contains 19 classes for training and evaluation. In our experiments, we only use 5,000 fine-annotated images. There are 2,975 images for training, 500 images for validation, and 1,525 images for testing. Note that the ground truth of testing set is unavailable, we shall submit the results to an online test server. Due to the limited physical memory, we randomly subsample image resolution to  $1,024 \times 512$  patches for training.

TABLE IV
ABLATION STUDIES ON BACKBONE CHOICES, #PAR: THE NUMBER OF
PARAMETERS, #NS: NETWORK SIZE.

Method	#Par(M)	#NS(MB)	MIoU(%)
FCN-VGG16	134.35	524.82	63.56
FCN-ResNet101	42.67	167.18	70.70
FCN-ResNet50	23.68	92.75	67.78
FCN-ResNet18	11.30	44.19	66.82
FCN-DenseNet121	7.09	28.11	68.41
FCN-MobileNet V2	1.93	7.68	67.55

**CamVid Dataset.** The CamVid is another urban scene understanding database [32] which contains 12 classes in total. It consists of 367 frames, 101 frames, and 223 frames for training, validation, and test, respectively. The original frame resolution for this database is  $960 \times 720$ . Following the prior works [4], [12], we randomly subsample all images into  $480 \times 360$  resolution for training.

2) Metrics: Segmentation accuracy. The Mean Intersection over Union (MIoU) is commonly adopted for semantic segmentation accuracy. Suppose n is the number of classes, we can compute it as:

$$MIoU = \frac{1}{n} \sum_{i=1}^{n} \frac{p_{ii}}{\sum_{j=1}^{n} p_{ij} + \sum_{j=1}^{n} p_{ji} - p_{ii}},$$
 (13)

where  $p_{ij}$  is the number of pixels that belong to i predicted to class j,  $p_{ii}$  refers to the true positive.  $p_{ij}$  and  $p_{ji}$  refer to the false positive and false negative, respectively.

**Execution speed.** The amount of forward pass time in millisecond (ms) a network takes to process an image, which is usually measured by frames per second (FPS).

**Network parameters.** The number of parameters is calculated as the total number of weights and biases of each layer in network.

**Memory footprint.** The amount of storage space required to store the network parameters. A lightweight network should have much fewer memory footprint.

**Computation complexity.** The number of float-point operations (FLOPs) required to measure how quickly and effectively a CNN model works.

3) Training Details: We implement our experiments in Pytorch with NVIDIA 1080Ti GPU cards (11G per GPU). All ablation results are presented on Cityscapes val set. To avoid the over-fitting, we randomly scale images from 0.5 to 1.5 and left-right flip them for all datasets. Besides, we employ the mean subtraction and add a random rotation operation from -3 to 3 degrees during training process. Following the prior protocol [7], we set initial learning rate to 0.005 and employ "Poly" learning rate policy by  $1 - (\frac{iter}{max\_iter})^{power}$  with a power 0.9. In the end-to-end learning, the network is trained by using Stochastic Gradient Descent (SGD) optimization algorithm with mini-batch of 4, of which the momentum is 0.9 and weight decay is 5e-4. The pixel-wise cross-entropy error is applied as our loss fuction.

# B. Modified MobileNet V2

1) Ablation for Backbone Choices: Designing a novel backbone for a specific scenario at high resolution often re-

TABLE V
ABLATION STUDIES ON INFERENCE STRATEGY, OS: OUTPUT STRIDE.

OS = 8	OS = 16	OS = 32	MIoU(%)
			59.64
1			61.39
		√	60.75

TABLE VI
ABLATION STUDIES ON INFERENCE STRATEGY. HDRS: HYBRID
DILATION RATES STRATEGY IN OUR BACKBONE. DA: DATA
AUGMENTATION. FLOPS ARE ESTIMATED ON A 3 × 640 × 360 INPUT.

HDRS	DA	FLOPs(G)	MIoU(%)
{2, 2, 4, 4}		0.031▲	66.15(6.51▲)
{1, 2, 3, 5}		0.025▲	66.17(6.53▲)
{2, 3, 5, 7}		0.048▲	67.86(8.22▲)
$\{3, 5, 7, 11\}$		0.083▲	69.41(9.77▲)
$\{2, 3, 5, 7\}$		0.048▲	68.13(8.49▲)

quires expensive training from scratch, so we adopt pretrained MobileNet V2 and compare it with other backbones that are widely adopted in current segmentation models. For fairness, all settings conformably follow our training protocol on FCNbased model. As shown in Table IV, FCN-VGG16 is obviously not comparable to FCN-Mobilenet V2 in both accuracy and model complexity. Even though FCN-ResNets achieve a similar or better performance compared with FCN-MobileNet V2, they are generally huge with respect to parameters and memory footprint. Additionally, we observe that FCN-DenseNet121 is a pretty good choice, which yields a solid accuracy of 68.41% MIoU, while the requirement of resources is far less than FCN-ResNets. Although FCN-MobileNet V2 has a slight decrease in accuracy, it seems to be more cost-effective than the former, which delivers about 4 times parameters reduction. To sum up, these comparisons demonstrate that MobileNet V2 based network efficiently brings great benefit to feature extraction.

2) Ablation for Output Stride: In this part, we conduct several experiments to explore a reasonable output stride. Due to a high-resolution image of  $3 \times 2,048 \times 1,024$  limits GPU resources, we do not consider denser feature maps with output stride = 4. As seen in Table V and Fig. 6, employing output stride = 16 or 32 attains a bit higher accuracy than output stride = 8, especially for confusing objects such as truck and bus (marked with green arrows). It reflects that successive sub-sampling layers could bring a sufficient field of view and make features more discriminative. Unfortunately, their performances in small objects such as pole and traffic light (marked with red arrows) are limited, owing to huge amounts of abandon details when utilizing output stride = 16 or 32. With a long-term consideration, the value of output stride is set to 8, so as not to make an irreversible affect for small objects recovery during inference.

3) Ablation for Dilation Strategy and Data Argumentation: To evaluate the effectiveness of dilation strategy in our backbone, we compare several proposals with the vanilla model where  $\{d_{stage4}, d_{stage5}, d_{stage6}, d_{stage7}\} = \{1, 1, 1, 1\}$ . As summarized in Table. VI, we find out that a) Compared with the original one, replacing the last four sub-sampling layers with dilation convolutions generally yields about 6%-

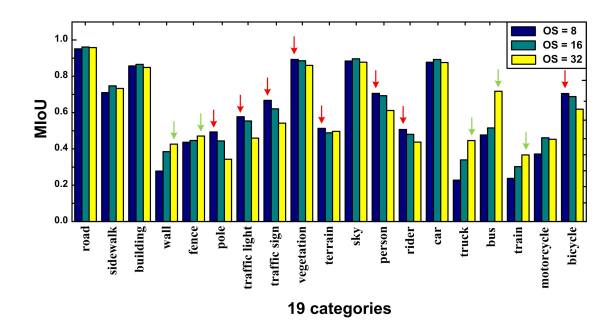


Fig. 6. The performance of 19 categories with different output stride on Cityscapes *val* set.

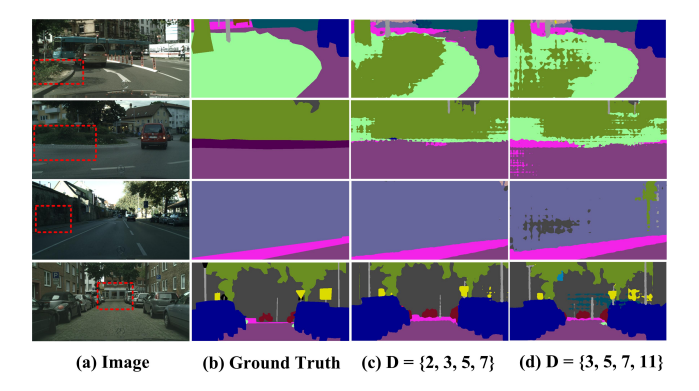


Fig. 7. Visualization results of "Gridding Effect" as a group of dilation rates goes larger and sparser. From left to right: Image, Ground Truth, the group of dilation rates  $\{2, 3, 5, 7\}$  and  $\{3, 5, 7, 11\}$  added into our backbone (best viewed in color).

10% MIoU boost, which denotes that this technique is more effective at an acceptable computation cost, b) Adopting  $\{d_{stage4}, d_{stage5}, d_{stage6}, d_{stage7}\} = \{2, 2, 4, 4\}$  indeed benefits the results, but it is not the best proposal. Due to same or geometric dilation ratios, the higher layer mostly samples information in the same region as the former one, thus making the field of view restricted, and c) As the group of dilation rates goes larger, the model facilitates a better result. However, the descriptor becomes too sparse to cover any relevant information, which requires more computation resources and leads to the aggravation of "Gridding Issue", as presented in red box of Fig. 7. We argue that this impact will mostly hinder the further improvement. Based on the above analysis, the costefficient case where  $\{d_{stage4}, d_{stage5}, d_{stage6}, d_{stage7}\} = \{2,$ 3, 5, 7} has been employed. Furthermore, results show that our naive baseline model with data argumentation yields even higher performance up to 68.13% MIoU.

### C. LRM and MCIM

Here we empirically study the effects of Long-skip Refinement Module and Muti-scale Contexts Integration Module.

1) Ablation for Long-skip Refinement Module: To reveal the effect of our LRM, we carry out several ablation studies as shown in Table VII. We first fix the semantic feature layer and vary the shallow feature layer, in order to measure the quality of different low-frequency information for feature refinement. As shown in the first three rows of Table VIII, they all outperform the baseline model, which demonstrates

TABLE VII

ACCURACY COMPARISONS WITH DIFFERENT LONG-SKIP MODULES.  $L_n$ : Low-frequency information outputted from n-th stage,  $n \in (1, 2, 3)$ .  $H_n$ : High-frequency information outputted from n-th stage,  $n \in (6, 7)$ . CA: Channel Attention.

Module	$L_1$	$L_2$	$L_3$	$H_6$	$H_7$	CA	Sum	MIoU(%)
а								68.44
b		√						68.39
c						$\sqrt{}$		68.72
d			$\sqrt{}$		$\sqrt{}$	$\sqrt{}$		68.51
e							$\checkmark$	68.23

#### TABLE VIII

Efficiency comparisons with different long-skip modules. FPT: Forward Pass Time.  $\sharp$ Par: The number of parameters. Note that FPT and FLOPs are estimated on a  $3\times640\times360$  input.

Module	FPT(ms)	#Par(M)	FLOPs(G)	MIoU(%)
а	0.8▲	0.007▲	0.010▲	0.31▲
b	0.9▲	0.009▲	0.016▲	0.26▲
c	0.3▲	0.010▲	0.020▲	0.59▲
d	0.9▲	0.025▲	0.042▲	0.38▲
e	0.1▼	0.007▲	0.020▲	0.10▲

the effectiveness of feature-refined strategy. As can be seen, module a and module b do not gain much benefit on the accuracy compared with module c. This indicates that although shallower features keep more details, the noise they have brought to the semantic features decrease the performance. In the case of module d, despite a similar benefit in accuracy, it imposes more than 2 times computation cost increase compared with module c, which is not a cost-efficient proposal. Moreover, module e shows that a straightforward sum of these features only yields 68.23% MIoU. Here leaves a question, why dose the long-skip learning seem to be useless? We think that an excessive gap existing between low-frequency and high-frequency features helps little for spatial information learning. In summary, module c yields the best boost of 0.59% MIoU only with 0.01 M extra parameters and 0.02 GFLOPs computation complexity increase, which illustrates a better trade-off than others. Fig. 8 visually shows that the LRM can benefit some small objects (e.g., pole, traffic sign).

2) Ablation for Dense Semantic Pyramid Block: To verify how different settings of K and r influence the result under the same condition, we comparatively measure their performances. For controlling the model size, we keep the number of feature maps outputted from each DSP block unchanged (output features = 200). Based on the results in Table IX, we come to several conclusions. On the one hand, with the number of descriptors K increases, model parameters and computation complexity is gradually lower, while facing the accuracy degradation from 71.02% to 70.10% MIoU. This result illustrates that excessive channel reduction will damage the performance due to large amounts of information loss. On the other hand, adopting multiple descriptors to capture different sub-regions near the target yields a MIoU of 0.50% boost, which proves that it delivers a stronger capacity of feature representations. To make a further step towards feature discrimination, learning global contexts yields about 0.55% MIoU improvement compared with the one without GAP. Based on these observations, we suppose a more cost-efficient

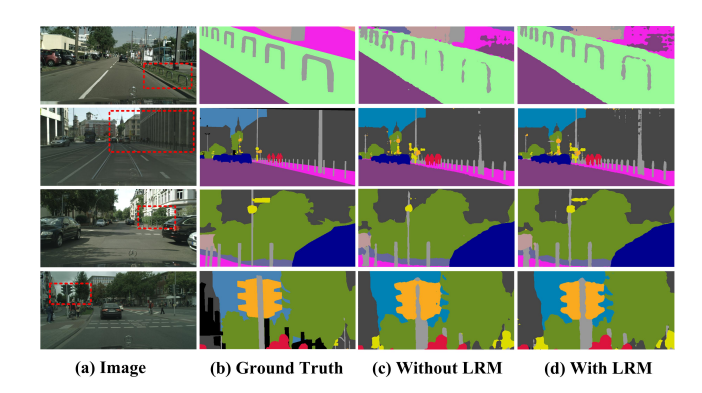


Fig. 8. Visualization results of the LRM on Cityscapes *val* set. From left to right: Image, Ground Truth, Without LRM, With LRM (best viewed in color).

strategy with K set to 4 and r set to 0.2, which only requires 0.06 M parameters and 1.79 GFLOPs computation complexity at a higher accuracy of 71.80% MIoU.

- 3) Ablation for Multi-scale Contexts Integration Module: We further investigate the effect of DSP blocks in parallel. As shown in Table X, in comparison with the DSP(C) module, the accuracy of MCIM(P) is improved from 71.80% to 72.34%, which indicates that the one in cascade suffers from the feature degradation as the network goes deeper. To overcome this problem, we add image-level features into our module to enhance the model learning capacity. With abundant global information, MCIM(C) achieves 72.02% MIoU eventually. In the following, the overall properties of both MCIM(C) and MCIM(P) will be analyzed.
- 4) Comparison with Similar Multi-scale Modules: We further investigate several powerful yet computationally expensive multi-scale modules in comparison with ours. The last two rows in Table XI reveals that MCIMs drastically reduce the number of parameters and simplify the computation complexity while maintaining a competitive accuracy. Specifically, MCIMs show a speed-faster performance with at most 43 times decrease in parameters and 128 times reduction in FLOPs jointly compared with Vortex and ASPP. In the case of FPA and PPM, they deliver a similar accuracy as ours, while suffering from heavier overheads (with at least 10 times parameters and 14 times computation increase) as well. These defects indicate that current multi-scale modules face the challenge of large amounts of time-consuming operations and invalid computation. Furthermore, it is obvious that MCIM(P) obtains a slight better accuracy than MCIM(C), due to the former adopts a wider module design for increasing the learning capacity (as demonstrated in [40]). Nevertheless, the "deep and thin" design of MCIM(C) leads to about 2.4 times parameters decrease and 5.6 times FLOPs reduction compared with the former. From all the above results, we prefer a more cost-efficient MCIM(C) and the MCIM(P) is regarded as a suboptimal choice. Fig. 9 presents some visual examples where some confusion categories exist. Obviously, with our MCIM, some analogous categories (e.g., wall and building, truck and bus) are correctly identified.

Finally, we provide the comparison of the baseline network and CIFReNet about loss and accuracy curves on CityScapes

#### TABLE IX

Comparisons of cascaded DSP blocks with different settings when adopting modified MobileNet V2 as backbone. K: The number of descriptors. r: Channel reduction ratio.  $D_k$  represents sampling scales of DSP $_k$  block,  $k \in (s, m, l)$ . GAP: Global Average Pooling.  $\sharp$ Par: The number of parameters. Note that FLOPs are estimated on a 320  $\times$  256  $\times$  128 input.

K	r	$D_s$	$D_m$	$D_l$	GAP	#Par(M)	FLOPs(G)	MIoU(%)
2	1/2	$\{6*K\}$	{12*K}	{18*K}		0.14	4.60	71.02(2.89▲)
4	1/4	$\{6*K\}$	$\{12*K\}$	$\{18*K\}$		0.08	2.43	70.75(2.62▲)
8	1/8	$\{6*K\}$	$\{12*K\}$	$\{18*K\}$		0.04	1.35	70.24(2.11▲)
16	1/16	$\{6*K\}$	$\{12*K\}$	$\{18*K\}$		0.02	0.76	70.10(1.97▲)
4	1/4	{1, 2, 3, 5}	{7, 9, 11, 13}	{17, 19, 21, 23}		0.08	2.43	71.25(3.12▲)
4	1/(4+1)	$\{1, 2, 3, 5\}$	{7, 9, 11, 13}	{17, 19, 21, 23}		0.06	1.79	<b>71.80</b> ( <b>3.67 ▲</b> )

TABLE X ABLATION STUDIES ON MCIMS. MCIM(C): DSP BLOCKS IN CASCADE. MCIM(P): DSP BLOCKS IN PARALLEL.

Method	MCIM	(C)	MCIM(P)	MIoU(%)
Wicthod	DSP(C)	GAP	WICHVI(I)	WHOC(70)
Baseline	√ ,	,	√	68.13 71.80(3.67▲) 72.34(4.21▲)
	√	$$		72.02(3.89▲)

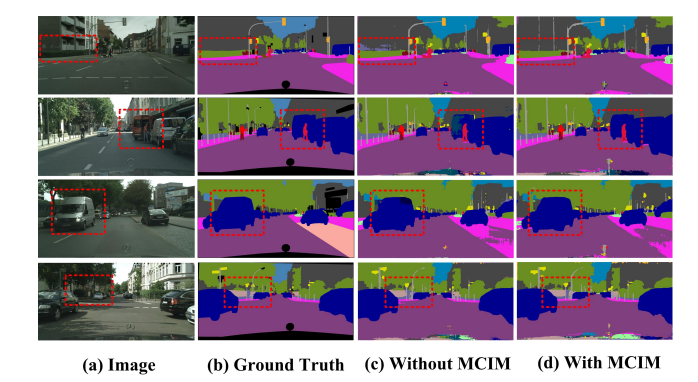


Fig. 9. Visualization results of the MCIM on Cityscapes *val* set. From left to right: Image, Groud Truth, Without MCIM, With MCIM (best viewed in color).

val set, as illustrated in Fig. 10(a) and Fig. 10(b). It reveals that our CIFReNet could achieve a better convergence and a higher accuracy than the baseline network. As shown in Table XII, our CIFReNet outperforms the baseline network by achieving a total of 4.82% MIoU promotion. In summary, both qualitative and quantitative results verify that the proposed two modules can effectively enhance network learning capacity.

## D. Evaluation on Cityscapes dataset

In this subsection, we compare our CIFReNet with other state-of-the-art methods, as displayed in Table XIII and Table XIV. The results are mostly evaluated on Cityscapes *test* set. "\*" represents the result on Cityscapes *val* set. We generally declare their execution speed estimated on a  $3 \times 1,024 \times 512$  input and FLOPs estimated on a  $3 \times 640 \times 360$  input. Additionally, "\*" represents that the speed is computed on an image of  $3 \times 625 \times 468$ . "•" and "o" represent that the FLOPs are computed on an image resolution of  $3 \times 512 \times 512$  and  $3 \times 1,024 \times 512$ , respectively. Execution Speed (ES) is averaged among 100 runs on NVIDIA TITAN X. Methods marked with "†" and "‡" represent results on a NVIDIA 1080Ti and other

TABLE XI

PERFORMANCE COMPARISONS WITH OTHER STATE-OF-THE-ART
MILITI-SCALE MODULES. FPT: FORWARD PASS TIME #PAR: THE

multi-scale modules. FPT: Forward Pass Time.  $\sharp$ Par: The number of parameters. Note that FPT and FLOPs are estimated on a  $320\times256\times128$  input.

Module	FPT(ms)	#Par(M)	FLOPs(G)	MIoU(%)
Vortex [31]	94.93	5.54	230.29	72.24(4.11▲)
ASPP [9]	59.60	4.52	174.86	71.72(3.59▲)
FPA [10]	27.60	7.48	43.30	72.02(3.89▲)
PPM [7]	19.38	1.28	25.21	70.92(2.79▲)
MCIM(P)	20.06	0.31	9.99	72.34(4.21▲)
MCIM(C)	20.73	0.13	1.80	72.02(3.89▲)

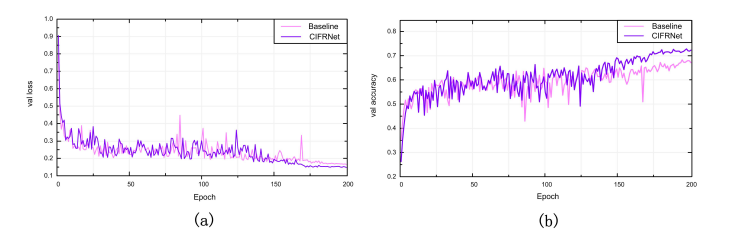


Fig. 10. The validation loss curve and accuracy curve of CIFReNet during 200 training epochs on CityScapes *val* set. (a) Validation loss vs. epoch. (b) Validation accuracy vs. epoch.

GPU cards, respectively. "-" indicates that algorithms have not published the corresponding value.

- 1) Performance Comparisons with Speed-fast Methods: As summarized in Table XIII, we report a comprehensive performance of CIFReNet compared with other speed-fast models. Several observations are as follows:
- a) With regard to accuracy-oriented approaches, some lightweight models such as SegNet [4], LinkNet [6], and SQ [11] have accelerated with great pace in speed, while failing to provide an accurate scene description for self-driving system. Besides, ENet [12] and Skip-Mobilenet [18] have excellent performance on model efficiency (e.g., execution speed, memory footprint or computation complexity) compared with ours. However, these methods only pursue efficiency by heavily compressing model, sacrificing too much accuracy as well. In contrast, our CIFReNet makes an obvious performance improvement by the powerful LRM and MCIM, which achieves 70.9% MIoU, and yields a real-time speed of 32.3 FPS on a 1,024 × 512 resolution image.
- b) Though these lightweight methods (e.g., GUN [14], LW-RefineNet [15], ERFNet [16], ICNet [17], and L-DenseNet [41]) have made a good trade-off between accuracy and speed, they do not give an adequate consideration on memory footprint and computation complexity. Differently, our CIFReNet

TABLE XII

ABLATION STUDIES ON LRM AND MCIM. LRM: LONG-SKIP
REFINEMENT MODULE. MCIM: MUTI-SCALE CONTEXTS INTEGRATION
MODULE.

Baseline	LRM	MCIM	MIoU(%)
			68.13
			68.72(0.59▲)
			72.02(3.89▲)
			<b>72.95(4.82</b> ▲)

TABLE XIII
PERFORMANCE COMPARISONS WITH OTHER SPEED-FAST METHODS ON
CITYSCAPES TEST SET.

Method	ES(FPS)	#Par(M)	FLOPs(G)	MIoU(%)
SegNet [4]	16.7	29.5	286.0	56.1
ENet [12]	76.9	0.4	3.8	58.3
LinkNet [6]	-	11.5	21.2	58.6
SQ [11]	16.7	-	-	59.8
Skip-Mobilenet <sup>‡</sup> [18]	45	3.4	6.2	61.5
ERFNet [16]	41.7	2.1	27.7	68.0
ICNet [17]	46.3	26.5	-	69.5
GUN <sup>‡</sup> [14]	33.3	-	-	70.4
LW-RefineNet <sup>†</sup> [15]	36.8*	46	52 <b>•</b>	72.1
L-DenseNet [41]	31	9.8	-	72.8*
CIFReNet†(Ours)	40*/32.3	1.9	8.1•/7.1	72.9*/70.9

TABLE XIV
PERFORMANCE COMPARISONS WITH OTHER HIGH-ACCURACY METHODS
ON CITYSCAPES TEST SET.

Method	ES(FPS)	#Par(M)	FLOPs(G)	MIoU(%)
DSPNet <sup>‡</sup> [42]	14.0	144.4	-	64.9*
FCN8s [22]	2	0.4	136.2°	65.3
Dilation10 [43]	0.25	140.8	-	67.1
DRN [44]	-	20.6	355.2°	67.3
LRR-4x [45]	-	-	-	69.7
DeepLab V2 [8]	0.25	44.0	457.8°	70.4
DLC [46]	-	26.5	-	71.1
FRRN [47]	0.25	-	235°	71.8
RefineNet [5]	0.9	118.1	-	73.6
DenseASPP121 [29]	-	28.6	155.8°	76.2
PSPNet [7]	0.5	70.4	453.6°	78.4
CIFReNet <sup>†</sup> (Ours)	40*/32.3	1.9	16.1°/7.1	72.9*/70.9

takes full advantages of compression techniques to relieve the resource burden, while substantially surpassing almost all algorithms stated above in accuracy. Particularly, the number of parameters and computation complexity are significantly reduced to only 1.9 M and 7.1 GFLOPs, which seems to be more resource-saving.

2) Performance Comparisons with High-accuracy Methods: Table XIV displays our results compared with high-accuracy methods. In particular, PSPNet [7], RefineNet [5], and Dilation10 [43] employ costly VGGs-like or ResNets-like base network, which take more than 2 seconds to predict segmentation results. Compared with these non-real-time algorithms, our CIFReNet achieves a significant progress both in speed and computation cost when working with high resolution images, and obtains a similar or slightly better accuracy to most of them (e.g., DeepLab V2 [8], DLC [46], and FRRN [47]). Without any auxiliary operations (e.g., Dense CRF [8]), our CIFReNet that only trained on fine annotation data reaches an impressive trade-off among overall properties for urban scene parsing. Fig. 11 presents some visual examples

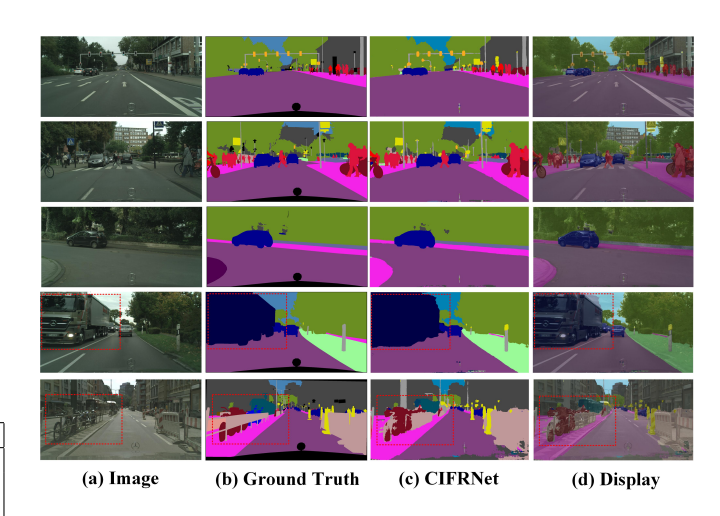


Fig. 11. Qualitative results on Cityscapes *val* dataset when employing our best model (best viewed in color). The last two rows show some failure cases.

 $\begin{tabular}{ll} TABLE~XV\\ PERFORMANCE COMPARISONS ON CAMVID TEST SET. \end{tabular}$ 

Module	#Par(M)	MIoU(%)
SegNet [4]	29.5	46.4
DeconvNet [48]	252	48.9
ENet [12]	0.4	51.3
LinkNet [6]	11.5	55.8
FCN8s [22]	134.5	57
Skip-Mobilenet [18]	3.4	58.8
FC-DenseNet56 [49]	1.5	58.9
DeepLab-LFOV [50]	37.3	61.6
Dilation10 [43]	140.8	65.3
CIFReNet(Ours)	1.9	64.5

on Cityscapes *val* set. As we can see, our CIFReNet suffers from commonly challenging issues such as smooth boundary or obscure objects, which we would deal with in future works.

#### E. Evaluation on Camvid dataset

We further evaluate CIFReNet on Camvid *test* set. Compared with Cityscapes dataset, the image resolution in Camvid dataset is much smaller, so that we set  $D_s = \{1, 2, 3, 5\}$ ,  $D_m = \{5, 7, 9, 11\}$ , and  $D_l = \{11, 13, 15, 17\}$  in three DSP blocks to effectively gather information from low-resolution feature maps. As reported in Table XV, we observe that the CIFReNet achieves 64.5% MIoU with only 1.9 M parameters, which facilitates a better trade-off between accuracy and model efficiency than efficiency-oriented (e.g., SegNet [4], ENet [12], and Skip-Mobilenet [18]) or accuracy-oriented (e.g., Dilation10 [43], DeepLab-LFOV [50]) methods. Some qualitative results on Camvid val set are shown in Fig. 12.

## V. CONCLUSION

In this paper, we present a lightweight Context-Integrated and Feature-Refined Network (CIFReNet) for urban scene parsing. Specifically, our method consists of two core components: Long-skip Refinement Module (LRM) and Multi-scale Contexts Integration Module (MCIM). The LRM is designed to provide a highway for low-frequency information flow and

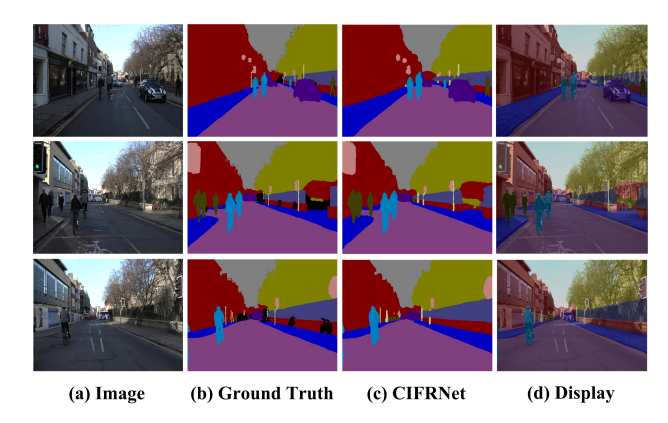


Fig. 12. Qualitative results on Camvid *val* dataset when employing our best model (best viewed in color).

boost the feature refinement efficiently. The MCIM utilizes Dense Semantic Pyramid (DSP) blocks and global features to exploit diverse contextual information and obtain sizeable field of view in an economical way. Theoretical analysis, ablation experiments, and result visualization demonstrate that our proposed CIFReNet not only gives precise segmentation results but also relieves the burden of execution speed and resources utilization, which makes it of great potentiality for deployment on resource-constrained intelligent devices.

In future works, we will make further discussions about two aspects: *a*) Regardless of the size of the dataset, a more robust model will be designed to show a steady performance at a faster speed. *b*) The issue on how to effectively enhance the performance of boundary prediction will be further explored, which is supposed to replace previous costly measures.

# REFERENCES

- A. Garcia-Garcia, S. Orts-Escolano, S. Oprea, V. Villena-Martinez, and J. Garcia-Rodriguez, "A Review on Deep Learning Techniques Applied to Semantic Segmentation," in Proc. the 27th International Conference on Computational Linguistics (COLING), 2018, pp. 2132-2144.
- [2] W. Hong, Z Wang, M Yang, and J. Yuan, "Implicit domain adaptation with conditional generative adversarial networks for depth prediction in endoscopy," in Proc. the 31th IEEE Conference on Computer Vision and Pattern Recognition (CVPR), 2018, pp. 1335-1344.
- [3] O. Ronneberger, P. Fischer, and T. Brox, "U-Net: Convolutional Networks for Biomedical Image Segmentation," in Proc. The 18th International Conference on Medical Image Computing and Computer-Assisted Intervention (MICCAI), 2015, pp. 234-241.
- [4] V. Badrinarayanan, A. Handa, and R. Cipolla, "SegNet: A Deep Convolutional Encoder-Decoder Architecture for Robust Semantic Pixel-Wise Labelling," IEEE Transaction on Pattern Analysis and Machine Intelligence, vol. 39, no. 12, pp. 2481-2495, 2015.
- [5] G. Lin, A. Milan, C. Shen, and I. Reid, "RefineNet: Multi-Path Refinement Networks for High- Resolution Semantic Segmentation," in Proc. the 30th IEEE Conference on Computer Vision and Pattern Recognition (CVPR), 2017, pp. 5168-5177.
- [6] A. Chaurasia, E. Culurciello, "LinkNet: Exploiting Encoder Representations for Efficient Semantic Segmentation," in Proc. the IEEE Visual Communications and Image Processing(VCIP), 2017, pp. 1-4.
- [7] H. Zhao, J. Shi, X. Qi, X. Wang, and J. Jia, "Pyramid Scene Parsing Network," in Proc. the 30th IEEE Conference on Computer Vision and Pattern Recognition (CVPR), 2017, pp. 6230-6239.
- [8] L. C. Chen, G. Papandreou, I. Kokkinos, K. Murphy, and A. L. Yuille, "DeepLab: Semantic Image Segmentation with Deep Convolutional Nets, Atrous Convolution, and Fully Connected CRFs," IEEE Transactions on Pattern Analysis and Machine Intelligence, vol. 40, no. 4, pp. 834-848, 2018.

- [9] L. C. Chen, Y. Zhu, G. Papandreou, F. Schroff, and H. Adam, "Encoder-Decoder with Atrous Separable Convolution for Semantic Image Segmentation," in Proc. the 15th European Conference and Computer Vision (ECCV), 2018, pp. 833-851, 2018.
- [10] H. Li, P. Xiong, J. An, and L. Wang, "Pyramid Attention Network for Semantic Segmentation," in Proc. the British Machine Vision Conference (BMVC), 2018, pp. 285.
- [11] M. Treml, J. Arjona-Medina, T. Unterthiner, R. Durgesh, F. Friedmann, and P. Schuberth, "Speeding up semantic segmentation for autonomous driving," in Proc. the 30th Conference on Neural Information Processing Systems Workshop (NIPSW), 2016.
- [12] A. Paszke, A. Chaurasia, S. Kim, and E. Culurciello. (2016). "ENet: A Deep Neural Network Architecture for Real-Time Semantic Segmentation." [Online]. Available: https://arxiv.org/abs/1606.02147
- [13] S. Mehta, M. Rastegari, A. Caspi, L. Shapiro, and H. Hajishirzi "ESPNet: Efficient Spatial Pyramid of Dilated Convolutions for Semantic Segmentation," in Proc. the 15th European Conference and Computer Vision (ECCV), 2018, pp. 561-580.
- [14] D. Mazzini, "Guided Upsampling Network for Real-Time Semantic Segmentation," in Proc. the British Machine Vision Conference (BMVC), 2018, pp.117.
- [15] V. Nekrasov, C. Shen, and I. Reid, "Light-Weight RefineNet for Real-Time Semantic Segmentation," in Proc. the British Machine Vision Conference (BMVC), 2018, pp. 125.
- [16] E. Romera, J. M. Ivarez, L. M. Bergasa, and R. Arroyo, "ERFNet: Efficient Residual Factorized ConvNet for Real-Time Semantic Segmentation," IEEE Transactions on Intelligent Transportation Systems, vol. 19, no. 1, pp. 263-272, 2017.
- [17] H. Zhao, X. Qi, X. Shen, J. Shi, and J. Jia, "ICNet for Real-Time Semantic Segmentation on High-Resolution Images," in Proc. the 15th European Conference and Computer Vision (ECCV), 2018, pp. 418-434.
- [18] M. Siam, M. Gamal, M. Abdel-Razek, S. Yogamani, and M. Jagersand, "RTSeg: Real-time Semantic Segmentation Comparative Study," in Proc. the IEEE International Conference on Image Processing (ICIP), 2018, pp. 1603-1607.
- [19] M. Sandler, A. Howard, M. Zhu, A. Zhmoginov, and L. C. Chen, "MobileNetV2: Inverted Residuals and Linear Bottlenecks," in Proc. the 31th IEEE Conference on Computer Vision and Pattern Recognition (CVPR), 2018, pp. 4510-4520.
- [20] Chollet, Francois, "Xception: Deep Learning with depth-wise Separable Convolutions," in Proc. the 30th IEEE Conference on Computer Vision and Pattern Recognition(CVPR), 2017, pp. 1800-1807.
- [21] X. Zhang, X. Zhou, M. Lin, and J. Sun, "ShuffleNet: An Extremely Efficient Convolutional Neural Network for Mobile Devices," in Proc. the 31th IEEE Conference on Computer Vision and Pattern Recognition (CVPR), 2018, pp. 6848-6856.
- [22] E. Shelhamer, J. Long, and T. Darrell, "Fully Convolutional Networks for Semantic Segmentation," IEEE Transactions on Pattern Analysis and Machine Intelligence, vol. 39, no. 4, pp. 640-651, 2014.
- [23] M. Cordts, M. Omran, S. Ramos, T Rehfeld, M. Enzweiler, R. Benenson, U. Franke, S. Roth, and B. Schiele, "The cityscapes dataset for semantic urban scene understanding," in Proc. the 29th IEEE Conference on Computer Vision and Pattern Recognition (CVPR), 2016, pp. 3213-3223.
- [24] M. Everingham, "The PASCAL Visual Object Classes Challenge (VOC2007) Results," Lecture Notes in Computer Science, vol. 111, no. 1, pp. 98-136, 2007.
- [25] D. Guo, L. Zhu, Y. Lu, and H. Yu, "Small Object Sensitive Segmentation of Urban Street Scene with Spatial Adjacency Between Object Classes," IEEE Transactions on Image Processing, vol. 28, no. 6, pp. 2643-2653, 2019.
- [26] R. Zhang, S. Tang, M. Lin, J. Li, and S. Yan, "Global-residual and local-boundary refinement networks for rectifying scene parsing predictions," in Proc. the 26th International Joint Conference on Artificial Intelligence (IJCAI), 2018, pp. 3427-3433.
- [27] H. Ding, X. Jiang, B. Shuai, A. Q. Liu, and G. Wang, "Context contrasted feature and gated multi-scale aggregation for scene segmentation," in Proc. the 31th IEEE Conference on Computer Vision and Pattern Recognition (CVPR), 2018, pp. 2393-2402.
- [28] R. Zhang, S. Tang, Y. Zhang, J. Li, and S. Yan, "Scale-Adaptive Convolutions for Scene Parsing," in Proc. the 16th IEEE Conference on IEEE International Conference on Computer Vision (ICCV), 2017, pp. 2050-2058.
- [29] M. Yang, K. Yu, C. Zhang, Z. Li, and K. Yang, "DenseASPP for Semantic Segmentation in Street Scenes," in Proc. the 31th IEEE Conference on Computer Vision and Pattern Recognition (CVPR), 2018, pp. 3684-3692.
- [30] M. Kampffmeyer, N. Dong, X. Liang, Y. Zhang, and E. P. Xing, "ConnNet: A Long-Range Relation-Aware Pixel-Connectivity Network

- for Salient Segmentation," IEEE Transactions on Image Processing, vol. 228, no. 5, pp. 2518-2529, 2019.
- [31] C. W. Xie, H. Y. Zhou, and J. Wu. (2018). "Vortex Pooling: Improving Context Representation in Semantic Segmentation." [Online]. Available: https://arxiv.org/abs/1804.06242
- [32] G. Brostow, J. Fauqueur, and R. Cipolla, "Semantic object classes in video: A high-definition ground truth database," Pattern Recognition Letters, vol. 30, no. 2, pp. 88-97, 2009.
- [33] A. Romero, N. Ballas, S. E. Kahou, A. Chassang, C. Gatta, and Y. Bengio, "Fitnets: Hints for thin deep nets," in Proc. the 3th International Conference on Learning Representations (ICLR), 2015.
- [34] Y. Zhang, K. Li, K. Li, L. Wang, B. Zhong, and Y. Fu, "Image Super-Resolution Using Very Deep Residual Channel Attention Networks," in Proc. the 15th European Conference and Computer Vision (ECCV), 2018, pp. 294-310.
- [35] J. Hu, L. Shen, S. Albanie, G. Sun, and E. Wu, "Squeeze-and-Excitation Networks," in Proc. the 31th IEEE Conference on Computer Vision and Pattern Recognition (CVPR), 2018, pp. 7132-7141.
- [36] S. Ioffe, C. Szegedy, "Batch Normalization: Accelerating Deep Network Training by Reducing Internal Covariate Shift," in Proc. the 32th International Conference on Machine Learning (ICML), 2015, pp. 448-456.
- [37] K. He, X. Zhang, S. Ren, and J. Sun, "Delving Deep into Rectifiers: Surpassing Human-Level Performance on ImageNet Classification," in Proc. The 15th International Conference on Computer Vision (ICCV), 2015, pp. 1026-1034.
- [38] P. Wang, P. Chen, Y. Yuan, D. Liu, Z. Huang, X. Hou, and G. Cottrell, "Understanding Convolution for Semantic Segmentation," in Proc. The IEEE Winter Conference on Applications of Computer Vision, 2017, pp. 1451-1460.
- [39] K. He, X. Zhang, S. Ren, and J. Sun, "Deep Residual Learning for Image Recognition," in Proc. the 28th IEEE Conference on Computer Vision and Pattern Recognition (CVPR). 2015, pp. 770-778.
- [40] S. Zagoruyko, N. Komodakis, "Wide Residual Networks," in Proc. the British Machine Vision Conference (BMVC), 2016.
- [41] I. Kreso, S. Segvic, and J. Krapac, "Ladder-style densenets for semantic segmentation of large natural images," in Proc. the 16th IEEE Conference on IEEE International Conference on Computer Vision Workshops (ICCVW), 2017, pp. 238-245.
- [42] L. Chen, Y. Zeng, J. Ma, and L. Zheng, "Driving Scene Perception Network: Real-Time Joint Detection, Depth Estimation and Semantic Segmentation," in Proc. The IEEE Winter Conference on Applications of Computer Vision (WACV), 2018, pp. 1283-1291.
- [43] F. Yu, V. Koltun. (2016). "Multi-Scale Context Aggregation by Dilated Convolutions." [Online]. Available: https://arxiv.org/abs/1511.07122
- [44] F. Yu, V. Koltun, and T. Funkhouser, "Dilated Residual Networks," in Proc. the 30th IEEE Conference on Computer Vision and Pattern Recognition (CVPR), 2017, pp. 636-644.
- [45] G. Ghiasi, C. C. Fowlkes, "Laplacian Pyramid Reconstruction and Refinement for Semantic Segmentation," in Proc. the 13th European Conference and Computer Vision (ECCV), 2016, pp. 519-534.
- [46] X. Li, Z. Liu, P. Luo, C. C. Loy, and X. Tang, "Not All Pixels Are Equal: Difficulty-aware Semantic Segmentation via Deep Layer Cascade," in Proc. the 30th IEEE Conference on Computer Vision and Pattern Recognition (CVPR), 2017, pp. 6459-6468.
- [47] T. Pohlen, A. Hermans, M. Mathias, and B. Leibe, "Full-Resolution Residual Networks for Semantic Segmentation in Street Scenes," in Proc. the 30th IEEE Conference on Computer Vision and Pattern Recognition (CVPR), 2017, pp. 3309-3318.
- [48] H. Noh, S. Hong, and B. Han, "Learning Deconvolution Network for Semantic Segmentation," in Proc. The 15th International Conference on Computer Vision (ICCV), 2015, pp. 1520-1528.
- [49] S. Jegou, M. Drozdzal, D. Vazquez, A. Romero, and Y. Bengio, "The One Hundred Layers Tiramisu: Fully Convolutional DenseNets for Semantic Segmentation," in Proc. the 30th IEEE Conference on Computer Vision and Pattern Recognition Workshops (CVPRW), 2017, pp. 1175-1183
- [50] L. C. Chen, G. Papandreou G, I. Kokkinos, K. Murphy, and A. L. Yuille, "Semantic Image Segmentation with Deep Convolutional Nets and Fully Connected CRFs," in Proc. the 3rd International Conference on Learning Representations (ICLR), 2015.